The International Journal of Advanced Manufacturing Technology (2019) 100:683–705
https://doi.org/10.1007/s00170-018-2540-6

ORIGINAL ARTICLE

Determining the relationships between the build orientation, process parameters and voids in additive manufacturing material extrusion processes

Hasti Eiliat[1] · Jill Urbanic[1]

Received: 27 February 2018 / Accepted: 7 August 2018 / Published online: 27 September 2018

Abstract
It stands to reason that the additive manufacturing build orientation for the material extrusion process affects the support material requirements, processing time, surface finish, etc. This paper aims to study the influence of the build orientation on the optimal process parameter settings (bead width, overlap, and raster angle), the amount, and location of unwanted voids. This research shows that there are limited optimal solution alternatives over the large solution space explored. The layer by layer process parameters are not selected independently. Knowledge of a void location in one layer is utilized to select a process parameter set for the next layer, preventing void regions from being stacked in 3D, and avoiding creating an internal chimney. Material extrusion processes, with a wide selection of nozzle sizes (0.4 mm to 21 mm), are considered suitable candidates for this solution. To carry out this study, a literature review was performed to understand the influence of the build parameters. Then, an analysis of valid parameter settings to be targeted was performed for a commercial system. The mathematical model is established based on the component geometry and the available build options for a given machine-material configuration. A C++ program has been developed to select a set of standards (available) toolpath parameters to determine the optimal process variables. Case studies are presented to show the merits of this approach. The influence of the orientation on the optimal process parameters is illustrated as well as its impact on voids. As expected, it is statistically shown that the amount and location of the voids depends on the build orientation. The optimal solution for the void minimization may be suboptimal for other criteria such as support material usage; consequently, a comprehensive multi-objective optimization heuristic algorithm needs to be developed. The processing time is long and is unacceptable for industrial applications. This outcome also needs to be addressed.

Keywords Material extrusion processes · Toolpath parameters · Void area · Void management · Build rotation · Additive manufacturing quality issues

1 Introduction

The material extrusion (AM-ME) process is one of the additive manufacturing (AM) (or 3D printing) processes. This process involves extruding beads of material placed side by side to create stacked layers to fabricate a component. This AM process family includes the fused deposition modeling (FDM) process [1], the large-scale additive manufacturing (LSAM) process [2, 3], the big area additive manufacturing (BAAM) process [4, 5], the medium area additive manufacturing (MAAM) process [3], and the small area additive manufacturing (SAAM) process [6], as well as many low-cost commercial systems being introduced in the market, such as the RepRap. Figure 1 illustrates representative achievable bead sizes for these AM-ME processes—other sizes are achievable with different nozzles and machine configurations. It can be seen that the selected bead widths can vary between 0.5 and 13 mm. With different nozzles, the bead width range can vary between 0.4 and 21 mm. The bead width and height are

✉ Hasti Eiliat
eiliath@uwindsor.ca

Jill Urbanic
jurbanic@uwindsor.ca

[1] Department of Mechanical, Automotive, & Materials Engineering, University of Windsor, 401 Sunset Avenue, Windsor, Ontario N9B 3P4, Canada

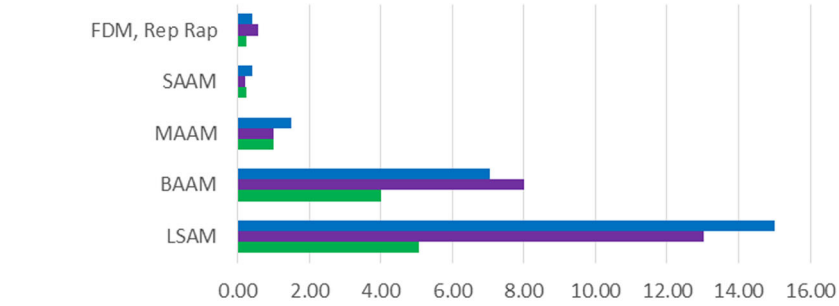

	LSAM	BAAM	MAAM	SAAM	FDM, Rep Rap
Nozzle Diameter (mm)	15.00	7.06	1.50	0.41	0.40
Bead Width (mm)	13.04	8.00	1.00	0.20	0.56
Bead Height (mm)	5.08	4.00	1.00	0.24	0.23

Fig. 1 Characteristics of different additive manufacturing material extrusion processes

coupled, typically in a 2:1 ratio. Consequently, there are extreme variants with the surface finish, build time, and the final component size for these material extrusion systems. These systems are used for a wide variety of applications in the classroom, health care, automotive, aerospace, and medical domains for both prototype and functional components.

The AM-ME process builds products by layering a material directly from a computer-aided design (CAD) model using the desired slice height and a standard bead width in a structured manner [7]. Thin wall covers, with vent holes, are utilized to illustrate the positive and negative characteristics with the AM-ME processes. The cover in Fig. 2 has a

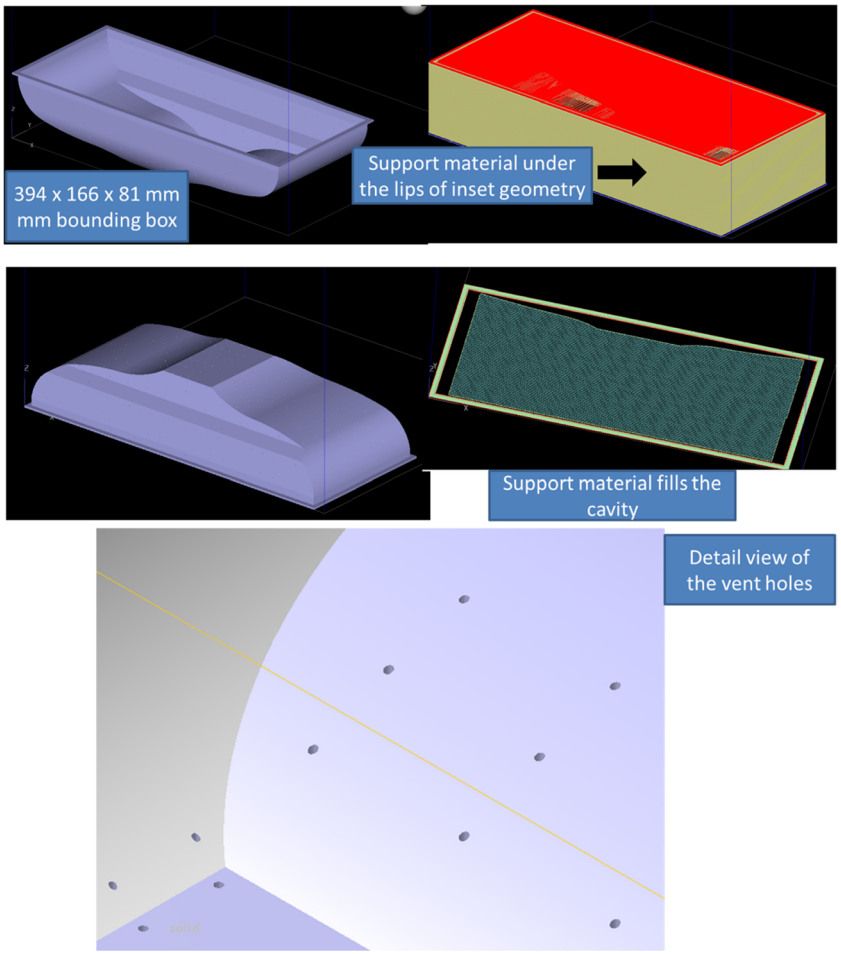

Fig. 2 Bottom vent cover geometry and material build estimates

Table 1 Comparison of time, build material, and support material for open face up and down of Fig 2.

0.178 mm slice thickness, 2:1 ratio bead thickness: bead height

Open face up	Solid, basic supports	Solid build and sparse support material	Open face down	Solid, basic supports	Solid build and sparse support material
Time	39 h 9 min	32 h 3 min	Time	58 h 44 min	34 h 59 min
Build (cm^3)	189.0	188.9	Build (cm^3)	228.2	208.3
Support (cm^3)	646.8	384.4	Support (cm^3)	1013.1	403.7
Total material	835.8	573.3	Total material	1241.3	612.0

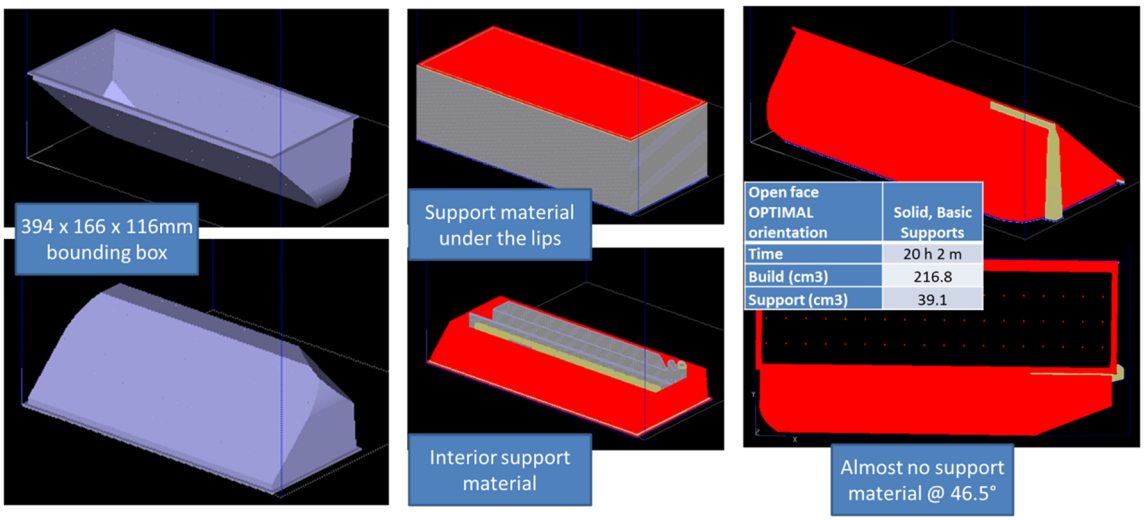

Fig. 3 Cover vent cover geometry, time, and material build estimates

large surface volume, and wall thicknesses that vary between 1.2 and 2.0 mm. The vent holes or slots have a 0.4-mm radius. The cover has a bounding box of 394 × 166 × 81 mm and 370 vent holes.

The build times are long for any build orientation, and there is support material required for overhanging structures (Table 1). The key positive characteristic for the AM process family is that complex components such as this part can be readily manufactured using an AM-ME machine for a moderately low-cost and moderate material waste compared to a machining solution; however, support material (here approximately 380–1010 cm^3) may be required. Consequently, support structure optimization has been designed to minimize support material requirements, as well as reduce part distortion, especially for thin wall projections.

A complementary venting cover (Fig. 3 and Table 2) clearly has an optimal build orientation, as there is one build orientation that minimizes support material and the total build time (Table 3).

Table 2 presents a comparison of the time, build material, and support material for the two positions shown in Fig. 3.

For many commercial systems, the designer does not select process parameters, such as the material feed rate or the travel speed. The only necessary process planning

Table 2 Comparison of time, build material, and support material for open face up and down of Fig. 3

0.178 mm slice thickness, 2:1 ratio bead thickness: bead height

Open face up	Solid, basic supports	Solid build and sparse support material	Open face down	Solid, basic supports	Solid build and sparse support material
Time	43 h 47 min	36 h 43 min	Time	48 h 33 min	37 h 12 min
Build (cm^3)	264.5	252.6	Build (cm^3)	278.7	251.1
Support (cm^3)	391.3	281.5	Support (cm^3)	576.6	304.3
Total material	655.8	534.1	Total material	855.3	555.4

Table 3 Comparison of time, build material, and support material for optimal position

Open face OPTIMAL	Solid, Basic Supports
Time	20 h 2 min
Build (cm^3)	216.8
Support (cm^3)	39.1
Total material	255.9

decisions focus on the resolution, or layer thickness, the component position and the orientation within the build envelope, and the general fill requirements. The process planning time is minimal. For the cover in Fig. 2, the four build options were generated in less than 10 min. The generated toolpath and the build parameters for the process are opaque to the user.

The AM-ME deposition toolpaths leave voids throughout the component, which impacts the strength and performance of the finished product. As Fig. 4 shows, a component can have different void positions when a different build orientation (XY plane versus the XZ plane) is utilized. In Fig. 4, the green color shows the toolpath for the specific layer and the red color illustrates the voids in that layer. It can be seen that there are numerous interior voids.

There are some methods such as computed tomography (CT) scans which can be utilized to observe and quantify voids within AM parts once they have been built [22]. However, there is a lack of predictive methodologies to visualize and quantify voids regions for various toolpath alternatives. Contemporary build solutions create unexpected and unwanted voids, which in turn creates a set of potential failure points within the finished product.

The goal of this paper is to explore the influence of the build orientation on the optimal process parameter settings (bead width, overlap, and raster angle), the amount, and location of unwanted voids and to determine the best build orientation for a maximum "fill" or minimum void condition for a given overlap threshold. An exhaustive search approach is taken. This is a partial extension of the research conducted to determine the optimal fill strategy for a localized region, layer, or layer set [8] for a component built with AM-ME processes. In the previous research, the boundary conditions are different, and one fixed build orientation is used. No new

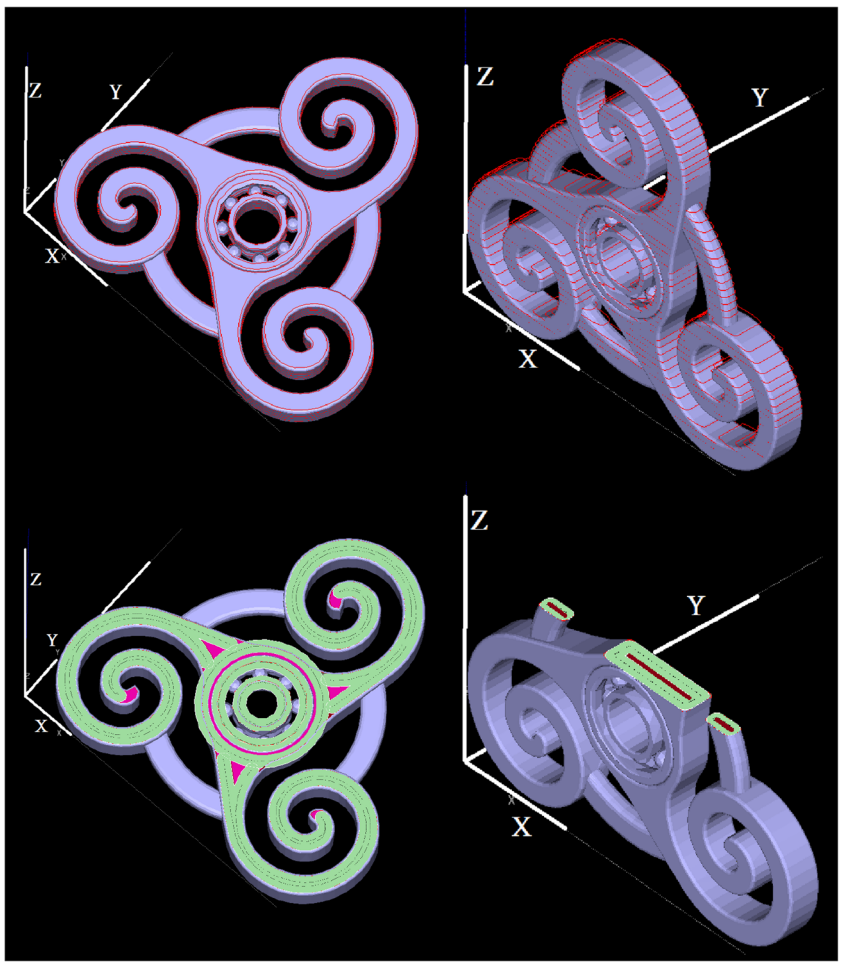

Fig. 4 Different rotations and positions of voids

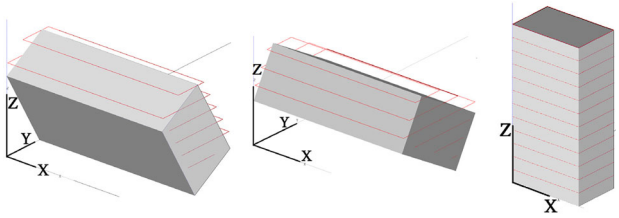

	(a)	(b)	(c)
# of Layers	47	41	80
Support Material (cm^3)	0.926	1.558	0.203
Build Material (cm^3)	1.929	2.317	1.475
Average Volume per Layer	0.041	0.057	0.018
Time (min)	13	18	9

Fig. 5 Different rotations of one part

toolpaths are created—contour and raster fill toolpath strategies along with existing process parameter to bead geometry relationships, already determined by the machine builder, are employed.

The component orientation in the build envelope influences the positions and areas for the voids. By changing the build orientation of the part, the number of slices and the cross sectional areas to be filled, along with the void regions within a component, will be different. Figure 5 shows the three different rotations for one part around the X- and Y-axes. As it is shown in the figure the number of layers, the area of each layer, the volume of support materials, and etc. are different between these build orientations. The bead height, bead width and raster angle for this example are 0.254 mm, 0.5064 mm, and 45°. Not only do voids need to be minimized within each layer, it is also important to reduce or eliminate void regions from being stacked contiguously in 3D, i.e., avoid creating an internal chimney. Again, this will be done by using available machine/process settings via comparing all build orientation solutions to select an optimal minimum total void configuration.

2 Literature review

There are five parameters which influence the toolpath and the resulting voids. These parameters are the bead width, the raster angle, the percent overlap, the bead height, and the build orientation. These parameters influence the fill strategy along with the unfilled or void regions, as well as the component strength and the surface finish.

Bead width A small bead width increases the build time significantly (Fig. 5), but it improves surface quality as it reduces the stair case effect [9]. It has been reported in the literature that a minimum bead width also improves strength [10]; however, this research does not consider

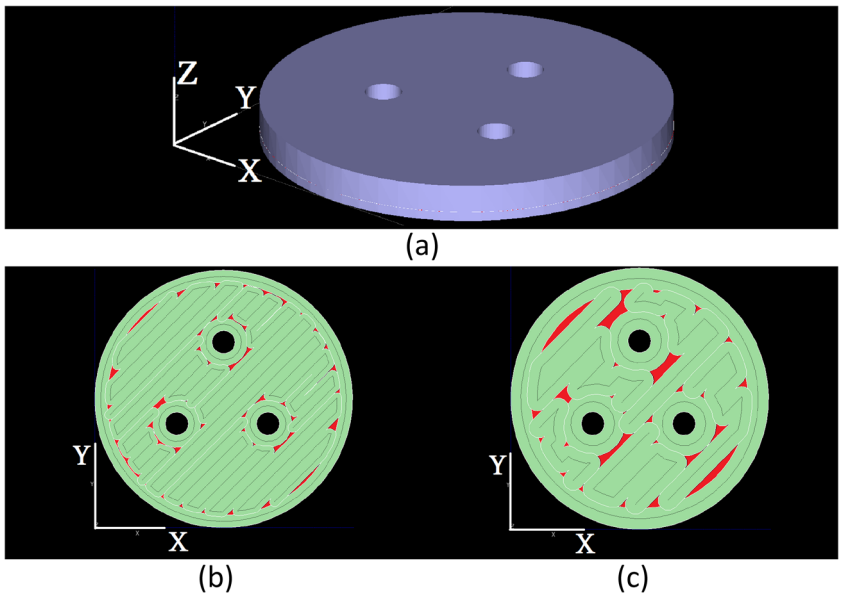

Fig. 6 Comparison of voids between two different bead width sizes, **a** 3D model, **b** layer with 0.4064 mm bead width, and **c** 0.8314 mm bead width

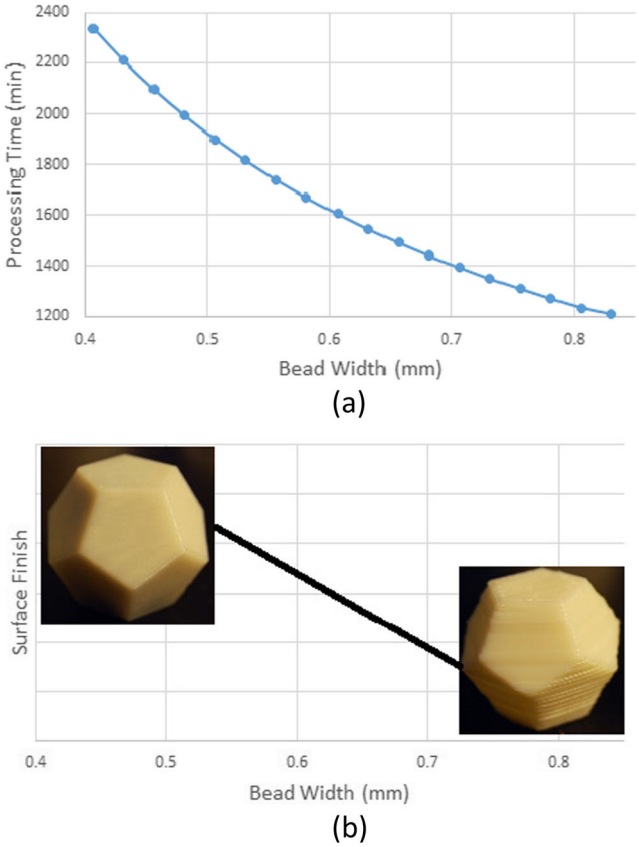

Fig. 7 **a**, **b** Relationship between the bead width with time and surface finish [20]

the influence of a partial fill condition. For example, Fig. 6a shows the cylinder with three holes, and Fig. 6b, c shows the filling condition with 0.4064 mm and 0.8314 mm bead width, respectively. As seen here, in both cases there are unwanted voids; consequently, both scenarios will have reduced mechanical properties.

The relationship between the bead width (for a set bead height) with time and surface finish are shown in Fig. 7, respectively. Therefore, not only the time, strength, and surface finish conditions should be considered when selecting a bead width. The void locations and size should also be considered.

Raster angle The raster angle is related to the world coordinate system of the machine. If the raster angle for the component build is aligned with the load direction, there is an improvement of tensile strength [10, 11]. However, when considering the build conditions in Fig. 6b, c, it is reasonable to expect lower mechanical strength characteristics for a raster fill aligned loading condition due to the interspersed voids.

Overlap The third parameter to be considered is the overlap percentage of the bead rasters. Rasters may touch side by side (a 0% overlap is the default for many machines), have a gap in between (a sparse or partial fill condition), or there may be an overlap condition. Increasing the overlap percentage can significantly improve the mechanical strength and stiffness [9, 10, 11, 12, 13]. For the overlap condition, conservation of mass must be considered—100% overlap is a "bead stacking" condition. A bounded or controlled overlap solution will be utilized in this research. The allowable overlap percentage values need to be defined for known for a bead shape, which could be modeled as an ellipse or an "obround" shape.

Bead height The fourth parameter to be considered is the bead height. Researchers have shown that the strength of the part decreases with increasing layer thicknesses. In the other words, a minimum viable bead height improves strength [10, 13, 14]. However, by minimizing bead height, all voids are not covered, even though usually a reduced bead width occurs with a smaller bead height (Fig. 8).

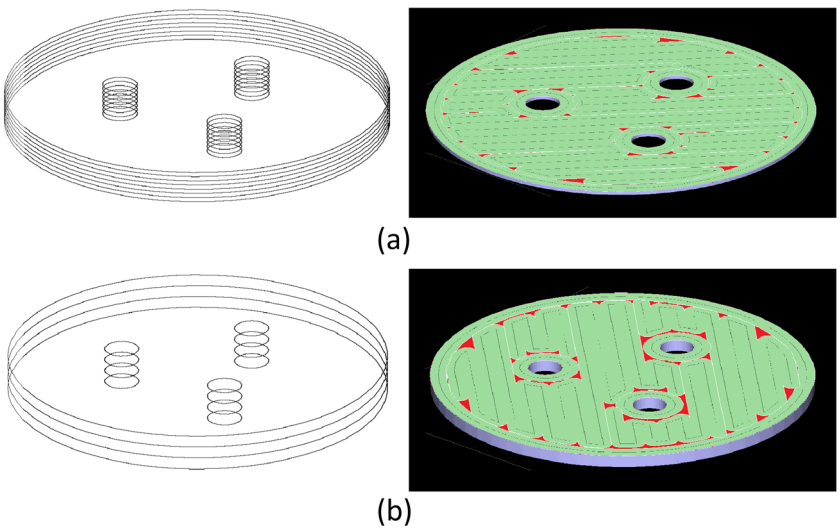

Fig. 8 Relationship between bead height and voids in the first layers. **a** Bead height 0.1270 mm. **b** Bead height 0.3302 mm

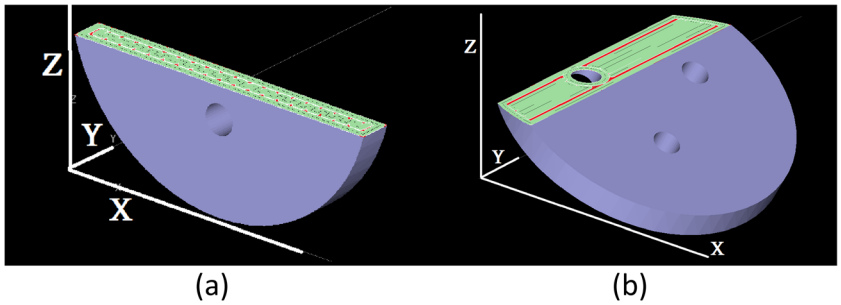

Fig. 9 Relationship between build orientation and voids **a** 90° around X-axis and **b** 30° around Y-axis

Orientation The build parameters and the resulting characteristics are interlinked. These results are also influenced by the build orientation. Figure 9 shows the voids in the 32nd layer for two cases, (a) 90° around X-axis and (b) 30° around Y-axis. The volume, position, and the shape of voids are influenced by the build orientation.

The build parameters are controlled by the Original Equipment Manufacturer (OEM) software for an AM-ME process solution. Table 4 presents some examples of OEM software in the market. Currently, none of these software solutions strategically maximizes the interior fill (or minimizes the voids), identifies/avoids internal stacked void regions or chimneys for a build orientation, or explores determining an optimal orientation when considering a fill strategy. In this table, the functions for each software are described. The Slicer function for the OEM software, such as the Cura software, prepares the selected model and generates the G-code for a machine. The 3D Printer Host function allows users to control and monitor all activities from the web browser and handheld machines. The 3D design and CAD function allows users to change the 3D model before printing the model. The STL Checker, STL Repair, and STL Editor Functions let users check, repair, and edit stl file during printing the model, respectively.

Minimizing the voids within a component is industrially relevant for both software developers/providers, and the end users. The research solutions presented in this paper can be readily implemented by the software solution providers listed in Table 4, as existing settings and toolpath strategies are being used, but in a strategic manner to reduce potential internal failure points. This is important to the end users, because they expect the performance characteristics of an injection molded part. There is now an understanding of the anisotropic problems associated with AM processes [9, 15], but there is no comprehensive appreciation of the problems associated with the numerous interior voids inherent in the AM-ME processes.

Table 4 OEM software for material extrusion processes [21]

Software	Function
Cura	Slicer, 3D Printer Host
CraftWare	Slicer, 3D Printer Host
Insight	Slicer, 3D Printer Host
Catalyst	Slicer, 3D Printer Host
123D Catch	3D Design, CAD
3D Slash	3D Design, CAD
TinkerCAD	3D Design, CAD
3DTin	3D Design, CAD
Sculptris	3D Design, CAD
ViewSTL	STL viewer
Netfabb Basic	Slicer, STL Checker, STL Repair
Repetier	Slicer, 3D Printer Host
FreeCAD	3D Design, CAD
Sketch Up	3D Design, CAD
3D-Tool Free Viewer	STL Viewer, STL Checker
Meshfix	STL Checker, STL Repair
Simplify3D	Slicer, 3D Printer Host
Slic3r	Slicer
Blender	3D Design, CAD
Mesh Lab	STL Editor, STL Repair
Meshmixer	STL Checker, STL Repair, STL Editor
OctoPrint	3D Printer Host

3 Mathematic model

In this section, the approach to determine an optimal build orientation, along with an optimal set of layer-based settings to have the least total amount of voids in all layers is

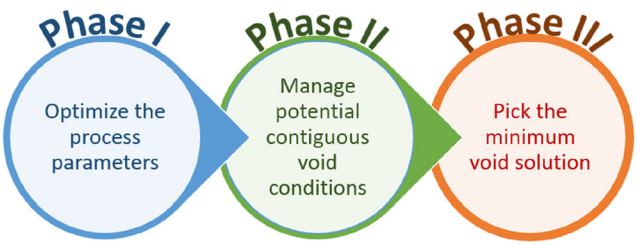

Fig. 10 Minimizing total voids in the material extrusion processes

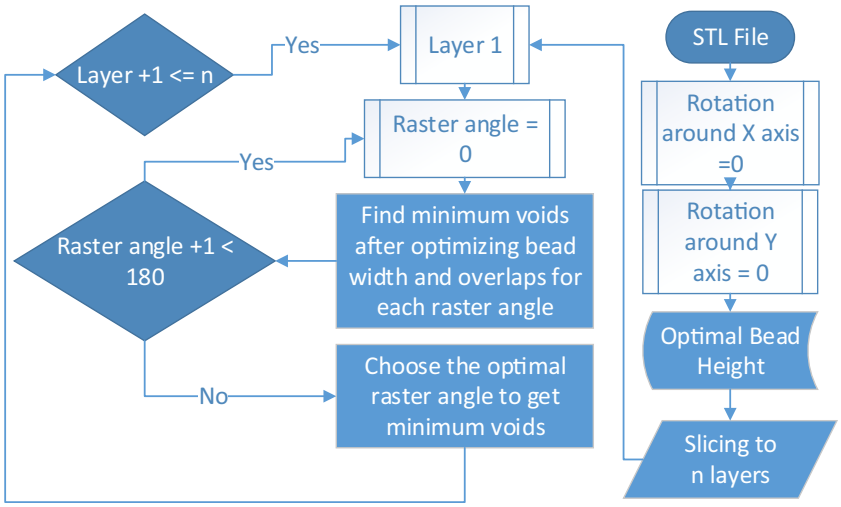

Fig. 11 Phase I process flow diagram

Table 5 Relationship between bead height and bead width for a Fortus 400 MC and the Insight® software

Bead height, $j \in J$ (mm)	Bead width, $i \in I$ (mm) $w_{i+1}^{j} = w_{i}^{j} + 0.025$		
0.1270	0.2032	⋯	0.5782
0.1778	0.3048	⋯	0.7298
0.254	0.4064	⋯	0.8314
0.3302	0.4572	⋯	0.9822

described. For a given orientation, bead height, and allowable overlap percentage range, the bead width, the raster angle, and the percent overlap are determined. As shown in Fig. 10, this solution approach consists of three phases.

3.1 Phase I—optimizing the process parameters—for an orientation

Figure 11 shows the phase I process flow diagram. The phase starts with uploading the stl file to the OEM software [16]. An *.stl file uses triangular facets to represent a shape, where each "facet" is defined in terms of the coordinates of its three vertices [17]. Thus, the edges and curves shapes seen as multifaceted shapes in the process [18]. This format can be sliced into a series of parallel cross-sections using simple line/plane intersection routines, which along with the specific process settings, is transparent to the user. The *.stl file decomposed to points and lines. The first position of the stl file in OEM software is assumed to have 0° rotation around X- and Y-axes.

It is assumed that the process parameters utilized for this optimization solution are existing process parameter configurations for an AM-ME machine and material set. These process parameters are related to each other. For example, the available bead width and bead height for a Fortus 400 machine with ABS material, which was developed by Stratasys in Eden Prairie, Minnesota [19], is presented Table 5. This table illustrates that each bead height has a range of bead widths. For example, if the optimal bead height will be 0.1778 mm then the available bead widths (mm) that can be used are {0.3048, 0.3298, 0.3548, 0.3798, 0.4048, 0.4298, 0.4548, 0.4798, 0.5048, 0.5298, 0.5548, 0.5798, 0.6048, 0.6298, 0.6548, 0.6798, 0.7048, and 0.7298}.

This data set is fixed, and is an input for this research. From these available and known process configurations, optimal process parameters such as the bead height, bead width, raster angle, and overlap percentages are determined. The

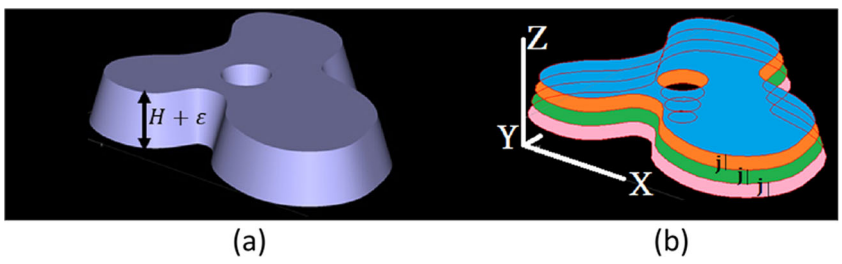

Fig. 12 Optimal bead height. **a** 3D model height. **b** Four layers with optimal bead height

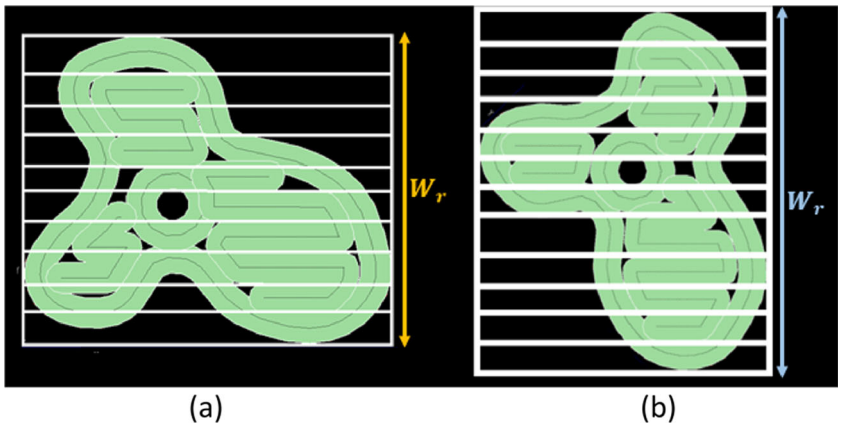

Fig. 13 W_r of one layer when the raster angle is **a** 0° and **b** 45°

mathematical formulation for determining each process parameter is explained in detail in the next subsections.

3.1.1 Bead height

Let j be the available bead height, and $N_j = \left\lceil \frac{H}{j} \right\rceil$ be an integer number layer with bead height j when the height of 3D model (during Z-axis) is H. If ε be the allowable part height tolerance, then for finding optimal bead height, equation below is used.

$$\begin{aligned} &\text{Maximize} && N_j \\ &\text{Subject to} && \frac{H}{j} \le N_j \le \frac{H+\varepsilon}{j}; \quad \forall j. \\ & && N_j \in \mathbb{N}^0; \quad \forall j. \end{aligned} \tag{1}$$

The above equation denotes that the height of the part needs to be less or equal than the allowable part height tolerance, and also the minimum bead height is preferred based on the facts that were explained in the literature review section. Figure 12 shows the 3D model with $H+\varepsilon$ height and with Eq. 1, the optimal bead height is j and N_j is four layers.

3.1.2 Bead width

Let w_i^j be the bead width $i \in I$ for the optimal bead height $j \in J$. As it is presented in Table 5, the bead height, j , has a range of discrete available bead widths, $i \in I$. Let W_r be the length between the lowest and highest points of the bounding rectangle around one layer with the raster angle, r , then

$$\begin{aligned} &W_r = y_r^{\max} - y_r^{\min}; \quad \forall r. \\ &y_r^{\max} = \max_{\forall l \in L} y_r^l; \quad \forall r. \\ &y_r^{\min} = \min_{\forall l \in L} y_r^l; \quad \forall r \end{aligned} \tag{2}$$

Figure 13a, b shows the difference of W_r when the raster angle is 0° and 45°. In these two cases, the size of optimal bead width are different due to the fact that W_r is depends on raster angle (r). The line spacing in Fig. 13 is uneven to show the difference between optimal bead widths in two cases.

3.1.3 Overlap percentage

Let O_i be the percentage of overlap with a bead width w_i^j and $R_i = \left\lceil \frac{W_r}{w_i^j} \right\rceil; \forall r, i, j$ be an integer number of rasters with a bead width w_i^j. The optimal overlap percentages for each allowable bead width is calculated by

$$O_i = \frac{R_i w_i^j - W_r}{w_i^j (R_i - 1)} * 100; \forall i, j, r \tag{3}$$

If O^* is the maximum allowable overlap in the process, then an optimal overlap need to be $O_i \le O^*$. Thus, for one

Fig. 14 Three categories of voids: **a** corner, **b** edge, and **c** contour island

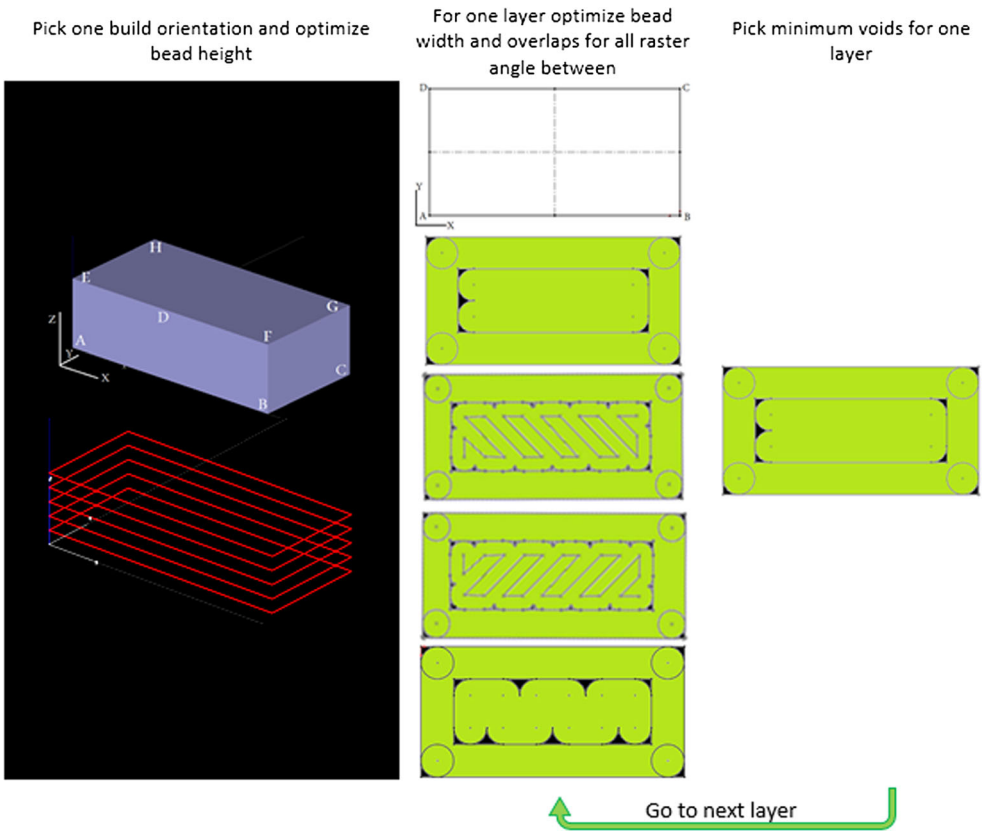

Fig. 15 Steps of phase I

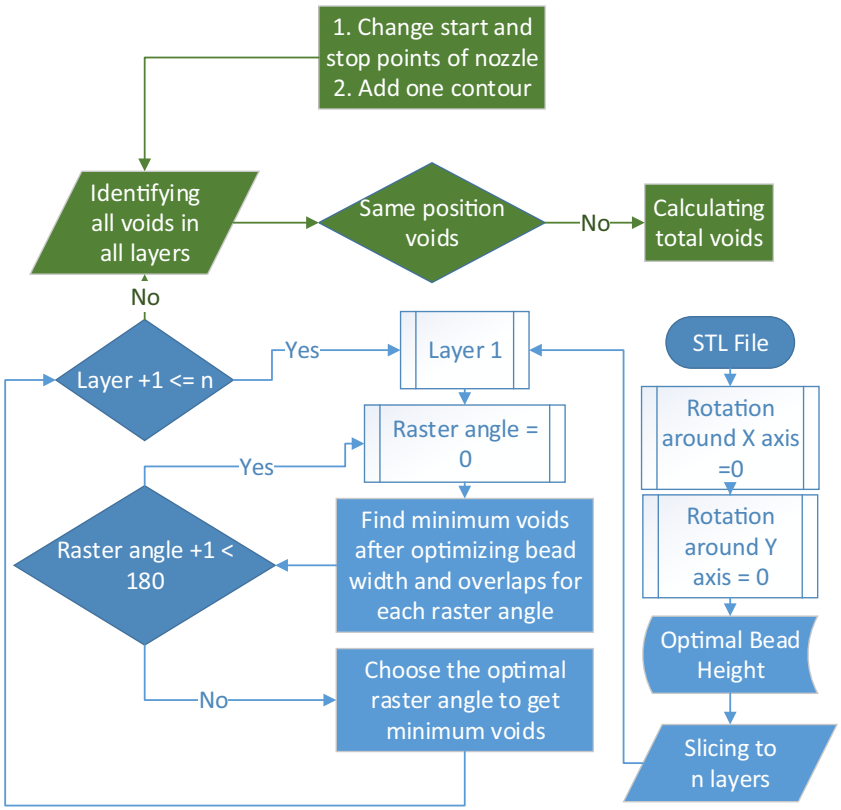

Fig. 16 Phase II diagram added to phase I diagram

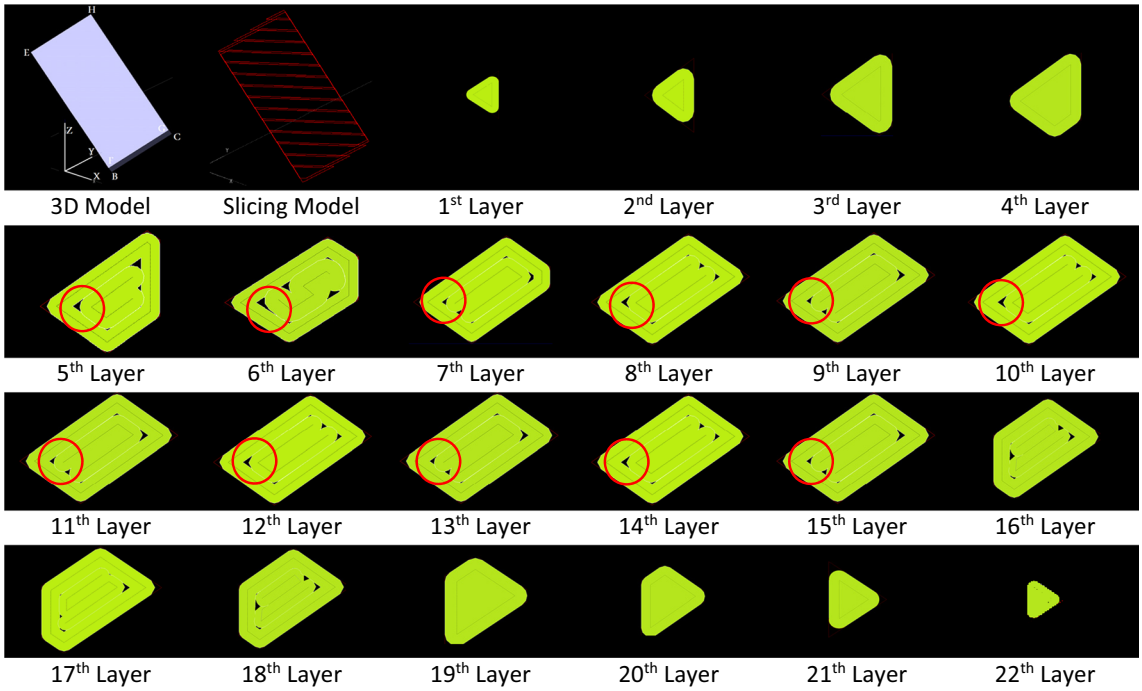

Fig. 17 Example for phase II

layer by changing the raster angle from 0° to 179°, there are 180 different W_r, and if the number of allowable bead width with bead height j is $\mathcal{N}$. Then for each raster angle there are $\mathcal{N}$ optimal bead width and $\mathcal{N}$ optimal overlaps with Eq. 3. For determining one optimal bead width and one optimal overlap for each layer, it is needed to calculate voids in each layer per raster angle.

3.1.4 Void areas

The voids that are generated using the AM-ME process are classified into three groups, which are shown in Fig. 14. The toolpath is shown as a green color, and the specific void type is shown as a red color.

Let $\hat{g}_l, \forall l \in L$ be the angle of corner $l \in L$ for the layer $q \epsilon Q$, and w_i^j be the bead width $i \in I$ for bead height, $j \in J$. Then the formula for calculating the corner voids area is

$$v_q^c = \sum_{l \in L} \left(\frac{w_i^j}{2}\right)^2 \left(\left| \cot \frac{\hat{g}_l}{2} \right| - \left(\frac{\pi - \hat{g}_l}{2}\right) \right); \ \forall i, j, q. \tag{4}$$

The second type of void is the edge void, v_q^E which is shown in Fig. 14b. The edge voids are dependent on the raster angle, the bead width and the overlap percentages. Let Ψ_t be the distance between y axes (y_l and y_{l+1}) of two continuous corners (l and $l+1$) in the layer q. $t \geq 1$ is for the corners which have $x_r^l > x_r^{\max}$ and $t \leq -1$ for $x_r^l < x_r^{\max}$ with raster angle $\hat{r}$. Let $\hat{e}_l$ be the angle between the edge l and the y axis and O_i is

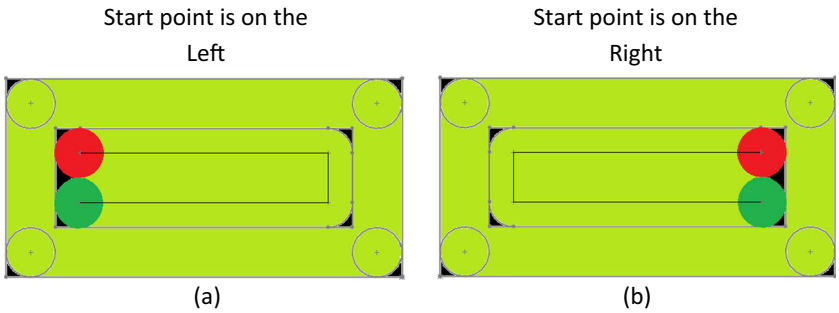

Fig. 18 Difference between voids when the start point of the nozzle is on the **a** left side or **b** right side

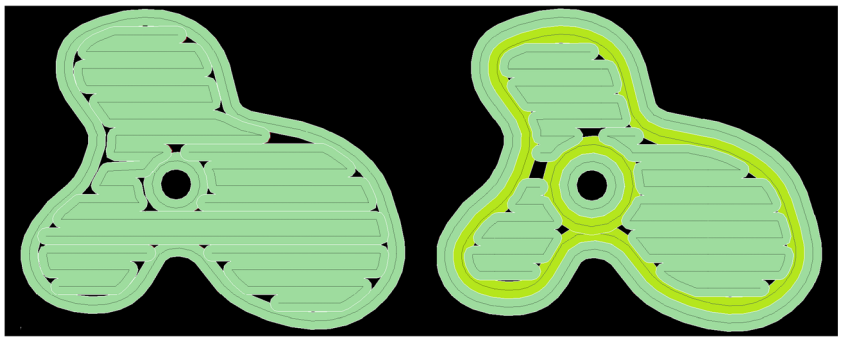

Fig. 19 (**a**) The voids for one layer that need to be covered by next layer, (**b**) adding one more contour to the next layer

optimal overlap. Edge l is the side between two corners of Ψ_t. Then the edge void, v_q^E, is calculated by

$$v_q^E = (1-O_i)\frac{w_i^{j2}}{4}\sum_{\forall l}\left\lceil\frac{\left\lceil\frac{\Psi_t}{w_i^j}\right\rceil}{2}\right\rceil\left(\frac{2}{\left|\mathrm{Sin}\widehat{e_l}\right|}-\frac{\pi}{2}\right);\forall i,j,\widehat{e_l}-\{0,\pi\},q \quad (5)$$

The third type of void is the "contour center" void. These voids occur when the contour toolpath is the only toolpath in the process and the contour geometry collapses upon itself. In this paper, it is assumed that there is one contour toolpath for each layer. It is recognized that strategically adjusting the number of boundary contours could position voids in areas determined to be less sensitive, but this is outside the scope of this research. The total void area of layer $q \epsilon Q$ with a raster angle $\hat{r}$, bead width w_i^j, and optimal overlap O_i, will be

$$\sum\left(v_q^c + v_q^E\right) \quad (6)$$

After comparing total voids with $\mathcal{N}$ bead width and overlaps for each raster angle, and then comparing 180 raster angles in each layer, the optimal bead width, overlap, and raster angle per layer are determined. Figure 15 summarizes phase I for the rectangular cube example. The rasters that are shown as an example for the layer are 0°, 45°, 135°, and 90°. For this specific example, the optimal raster angle to minimize voids in the layers is 0°.

3.2 Phase II—elimination of internal chimneys or 3D contiguous segments

The second phase targets determining the positions for the voids, and selecting a 'suboptimal' process parameter configuration needed to prevent void regions being stacked contiguously between layers (Fig. 16).

A simple example for a box rotated at a random orientation is used to illustrate this algorithm is presented in Fig. 17. For the optimal bead height in this scenario, the box is sliced into 22 layers. The voids in each layer are identified in this figure. It can be seen that there are regions where there will be a 3D chimney, which are circled in this figure.

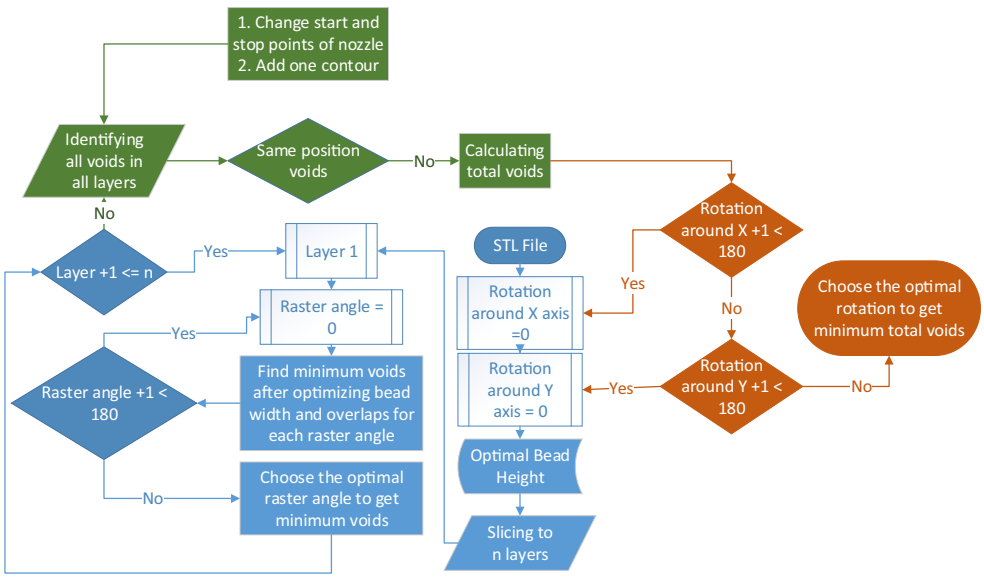

Fig. 20 Phase III diagram with the color code of Fig. 10, which is blue for phase I, green for phase II, and orange for phase III

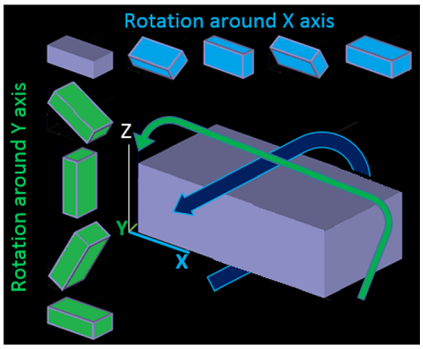

Fig. 21 Rotation around X- and Y-axes

Multiple approaches can be taken to cover the voids between layers. Choosing the optimal approach is dependent on the shape of the part. If the part is 2D extruded shape, then by changing the position of start point of nozzle from left to right between each layer all voids will be covered. For example, if the optimal layer for 2D extruded rectangular box is Fig. 18a, then the next layer on top of the previous layer should be Fig. 18b to cover voids in the previous layer.

However, in some 2D extruded cases or the other complex shapes, changing the start point of the nozzle does not address this issue. In these cases, one or more contours will be added to the specific layer-contour set to cover the voids in the previous layer. For example, for covering the voids in the layer that is shown in Fig. 19a, by adding one more contour to the next layer, all voids will be covered.

3.3 Phase III—finding an optimal build orientation to minimize voids

The process flow diagram related to determining an optimal orientation set (phase III) is shown in Fig. 20.

In this third phase, the part is rotated around X- and Y-axes, and the optimal build conditions determined. The total amount of rotations is 180^2: there are 0° to 179° rotations around the X-axis and 0° to 179° rotations around the Y-axis. If the stl file has θ_x angle about the X-axis and θ_y angle about Y-axis, then points in *.stl file is described as $\left(\mathcal{X}^{(\theta_x,\theta_y)}, \mathcal{Y}^{(\theta_x,\theta_y)}, \mathcal{Z}^{(\theta_x,\theta_y)}\right)$. Then if the *.stl file rotates $\left(\theta_x'-\theta_x\right)$ about X-axis and $\left(\theta_y'-\theta_y\right)$ about Y-axis, then the points will be changed to

$$\begin{bmatrix} x^{(\theta_{x'},\theta_{y'})} \\ y^{(\theta_x',\theta_y')} \\ z^{(\theta_x',\theta_y')} \end{bmatrix} = \begin{bmatrix} \cos\left(\theta_y'-\theta_y\right) & 0 & \sin\left(\theta_y'-\theta_y\right) \\ \sin\left(\theta_x'-\theta_x\right)*\sin\left(\theta_y'-\theta_y\right) & \cos\left(\theta_x'-\theta_x\right) & -\sin\left(\theta_x'-\theta_x\right)*\cos\left(\theta_y'-\theta_y\right) \\ -\cos\left(\theta_x'-\theta_x\right)*\sin\left(\theta_y'-\theta_y\right) & \sin\left(\theta_x'-\theta_x\right) & \cos\left(\theta_x'-\theta_x\right)*\cos\left(\theta_y'-\theta_y\right) \end{bmatrix} * \begin{bmatrix} x^{(\theta_x,\theta_y)} \\ y^{(\theta_x,\theta_y)} \\ z^{(\theta_x,\theta_y)} \end{bmatrix}; \quad (7)$$

$\forall \theta_x, \theta_y, \theta_x', and\, \theta_y'.$

Thus, with the above equation, all points, lines, and curves are defined in each rotation, as shown in Fig. 21. The algorithm for these phases is written in C++ and run for different cases studies and the results.

4 Case studies and results

This section illustrates two different case studies. The first case study is a toy car seat [8] and is an extension of previous

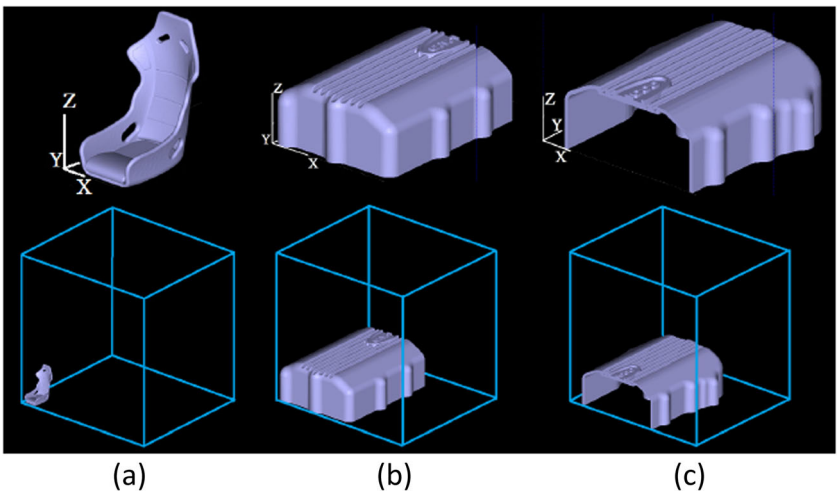

Fig. 22 Three case studies with 0° rotations around X- and Y-axes. **a** Toy car seat. **b** Valve cover I. **c** Valve cover II

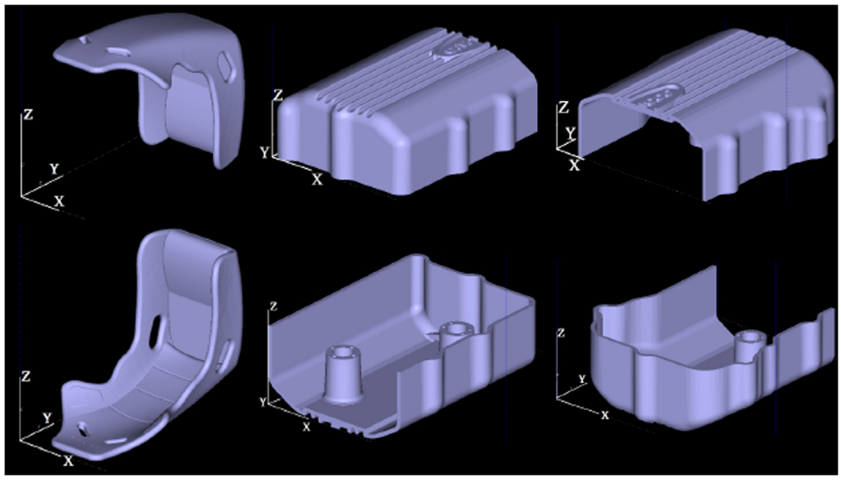

Fig. 23 The rotations which have the minimum voids

work. The other case study targets developing an optimal build condition for a valve cover pattern set to be used as patterns for sand casting. This is a "rapid tooling" application, and the achievable production volumes will be linked to the durability of the patterns. Consequently, determining optimal build conditions and a minimum void orientation is important. The difference of their sizes and the key features are shown in Fig. 22. The car seat is mm 13.59 × 17.24 × 21.26 cm, it has four non-planar slots, is symmetric in the along the Z-axis at the mid value along the X-axis, and has no flat surfaces The valve cover pattern is large—237.26 × 600 × 113.59 cm—and has internal features, which will result in multiple contours per layer, depending on the build orientation. The part sections are non-symmetric, but there are regions where the 2D extrusion geometry is consistent. There is surface detail, and it should have the best surface finish possible to be esthetically pleasing. The valve cover part is divided into two separate parts with 237.26 × 300 × 113.59 cm sizes. Figure 22 shows these case studies when they have 0° rotation about X- and Y-axes.

After performing the analyses, the optimal rotations for the case studies are shown in Fig. 23. The maximum allowable % overlaps for these cases are 50% and the bead widths and bead heights are determined from the set presented in Table 5.

Each of the optimal rotation for Fig. 23 has a specific optimal process parameter set for each layer. The toy car seat, Fig. 22a, in the optimal orientation has 68 layers with 0.1778 mm bead height. The optimal bead widths are between 0.3 and 0.5 mm. The valve cover, Fig. 22b, c, has 453 layers with a 0.254-mm bead height and the optimal bead widths are between 0.4 and 0.46 mm. Although, the maximum allowable

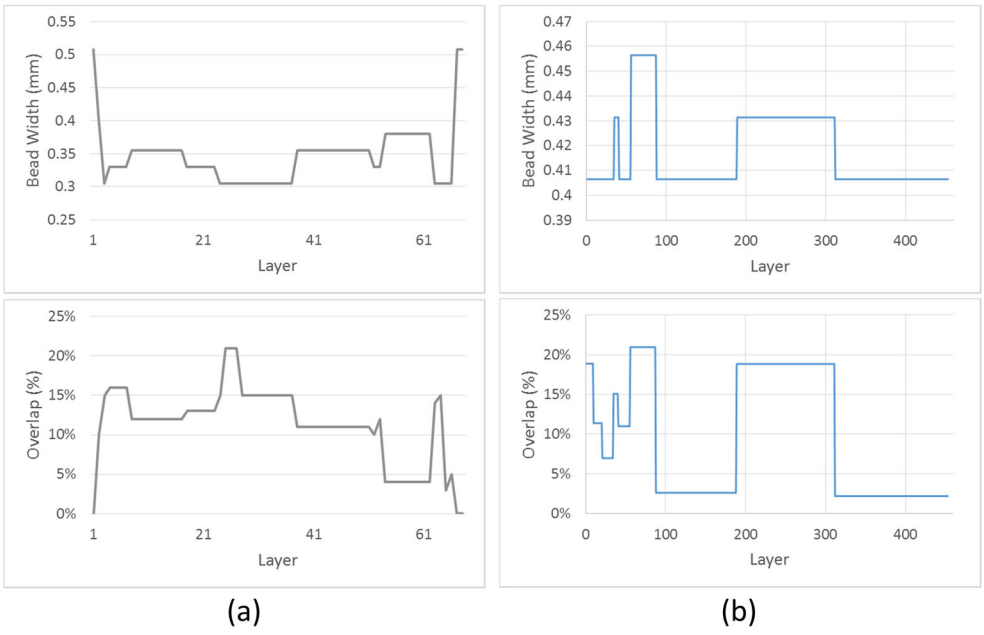

Fig. 24 Bead width and overlaps per layer for **a** car seat and **b** valve covers I and II

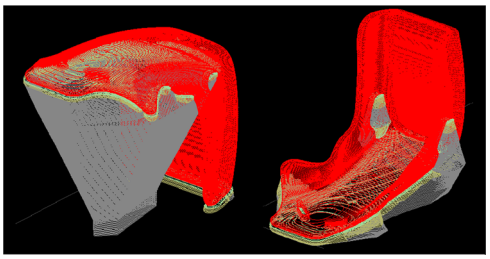

(a) (b)

Building time	4 hrs. 24 min	2 hrs. 43 min
Support material (cm^3)	31.212	12.892
Removing support material time	1 hr.	10 min

Fig. 25 Comparison of time and support material between two optimal orientations

overlap percentages for all cases is 50%, the optimal overlaps in these cases do not exceed 25% Fig. 24 (a) and (b). The reason for this result is that the model prefers to use the minimum bead width rather than a maximum overlap percentage.

For each specific case, there are two optimal rotations, as the results can be mirrored. To select the final build orientation, other factors, such as the surface finish or the required support material would need to be considered.

Figure 25 shows the difference between time and support material for two optimal build orientations for the car seat. In both rotations, the total void results are the same. As it can be seen, for producing Fig. 25a, the support material is

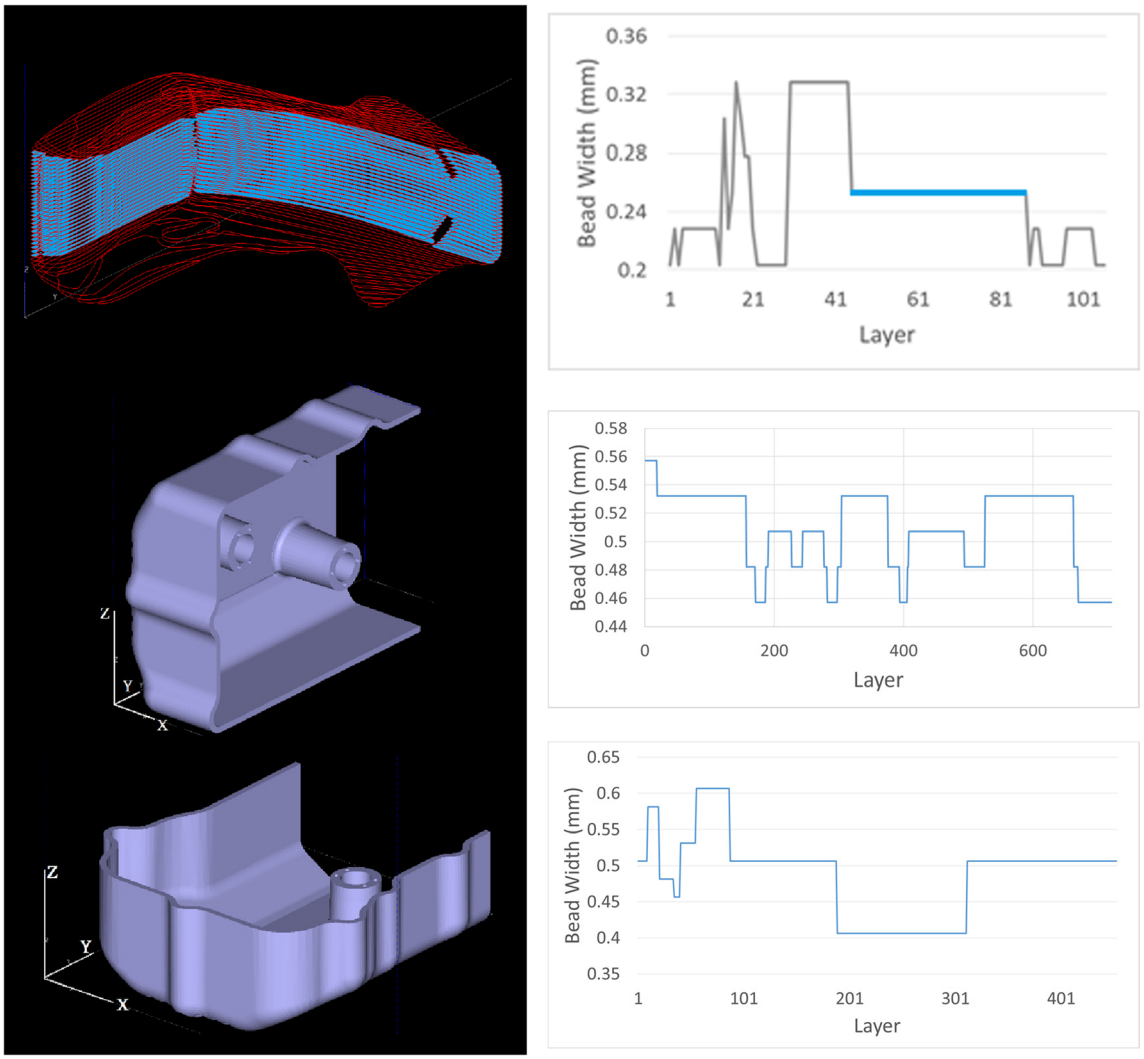

Fig. 26 Optimal rotations to minimize voids with overlap percent set to 0% for all case studies

Table 6 Comparing parameters when the allowable overlaps are 0% and 50%

	Car seat		Valve cover I		Valve cover I	
Overlap	0%	50%	0%	50%	0%	50%
Rotations (θ_x, θ_y)	(0°, 90°)	(90°, 0°)	(0°, 90°)	(0°, 0°)	(0°, 0°)	(0°, 0°)
Number of layers	106	68	721	453	453	453
Optimal bead height (mm)	0.127	0.1778	0.3302	0.254	0.254	0.254
Volume of voids (mm^3)	1.48	0.79	98.52	50.22	90.10	47.93
Volume of part (mm^3)	7.79	7.71	1005.33	1004.42	958.55	958.55
Percentage of voids	19%	13%	9.8%	4.9%	9.4%	5%

approximately three times more than the amount required in Fig. 25b. By using more support material, the building time and the time for removing the support material will be dramatically increased. The total processing time for Fig. 25a is around twice more than Fig. 25b. The other parameter for choosing between these two optimal rotations is surface finish. If the user needs to have the best surface finish on the seat depth and back of the seat, Fig. 25b will be preferred. However, if the surface finish of the seat back is to be considered, then Fig. 25a is the best choice.

For testing the solution variations generated by this new model, the allowable overlap percentage in the previous cases is changed from 50 to 0% (the standard build condition for commercial systems). The new optimal rotations, number of

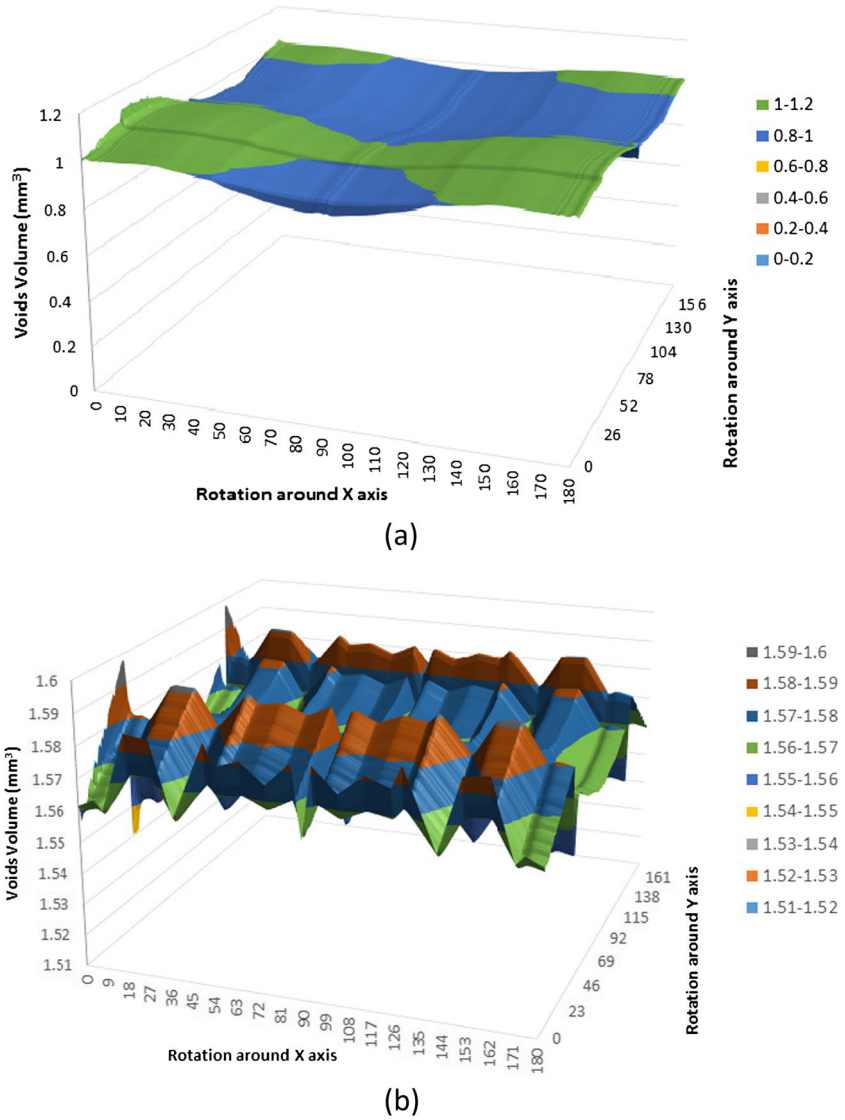

Fig. 27 Voids volume (mm^3) per rotation around X- and Y-axes for car seat with allowable overlaps. **a** 50%. **b** 0%

layers, and the range of bead widths for these cases are illustrated in Fig. 26. The regions where the planar slices are approximately the same (highlighted) result in constant bead widths (bold line in Fig. 26b) for the available build options.

Table 6 compares the case studies with two different allowable overlaps 0 and 50%. In this table, the volume of the part varies as there are different overlap percentages. Thus, the optimal bead height is changed, and the area of each layer is changed as well. The below table shows when the overlap is 50% the percentage of voids is less than when the allowable overlap is 0%.

5 Discussion

Figures 27a, b, 28a, b, and 29a, b illustrate the total voids per build rotation for the car seat, valve cover I, and valve cover II, respectively, when the allowable overlaps are 50% (a) and 0% (b). As these figures show, the voids where the allowable overlap percentage is 0% have significantly more fluctuation and ripples compared to the solution that allows for the 50% overlap condition. The reason is the only optimal bead widths and raster angles can be determined (phase I algorithm).

Although the car seat CAD model is symmetric, the solution surface is not due to the void stack elimination aspect of the algorithm (phase II).

For valve cover I, the void volumes are larger with the 0% allowable overlap condition than those with the 50% allowable overlap condition. In all cases, the range of voids increased when the allowable overlap limit is decreased. For example, for the valve cover I with a 50% allowable overlap, the range of voids is between 49.5 and 52 mm^3. However with a 0% allowable overlap, the range of voids changed to 52.5 mm^3 and 55 mm^3 (Fig. 28). The range of voids is very similar for valve cover II with the 50% allowable overlap (45 mm^3 and 52 mm^3). However, for the 0% allowable overlap scenario, the void range changes significantly to 88 mm^3 and 95 mm^3. The encircled spike has the same shape and general location in the surface graph, but the resultant void magnitudes are different.

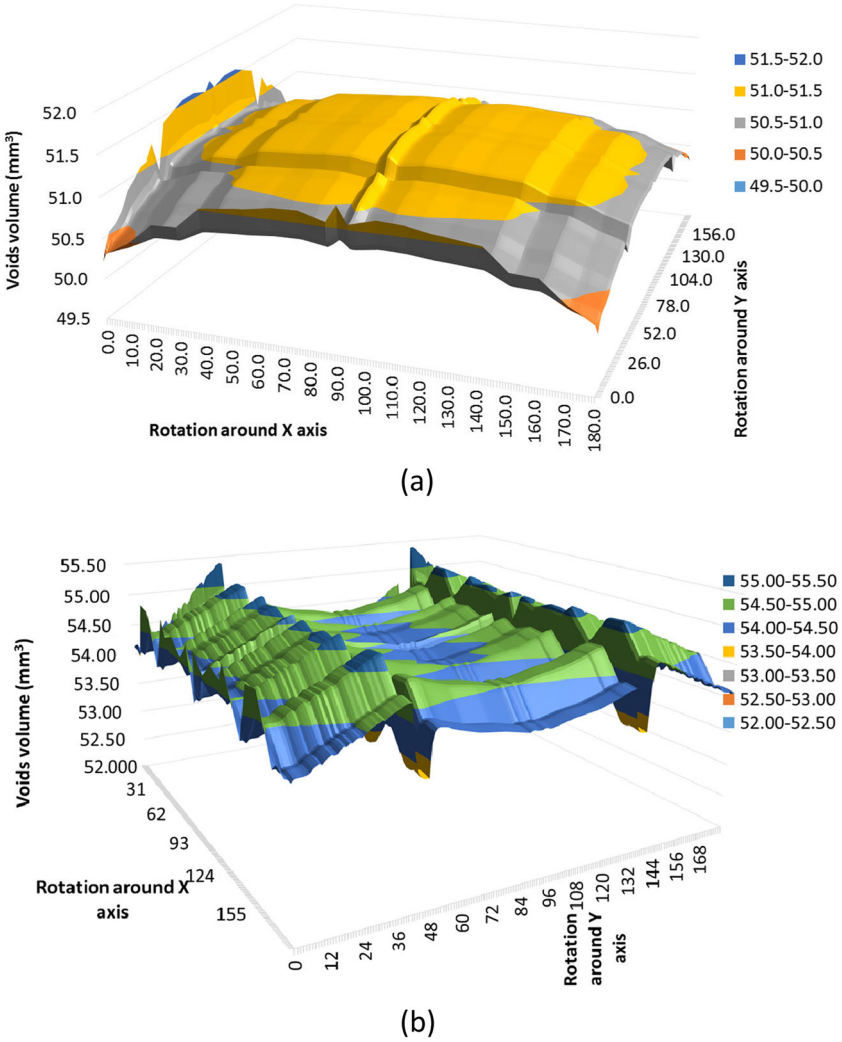

Fig. 28 Voids volume (mm^3) per rotation around X- and Y-axes for valve cover I with allowable overlaps. **a** 50%. **b** 0%

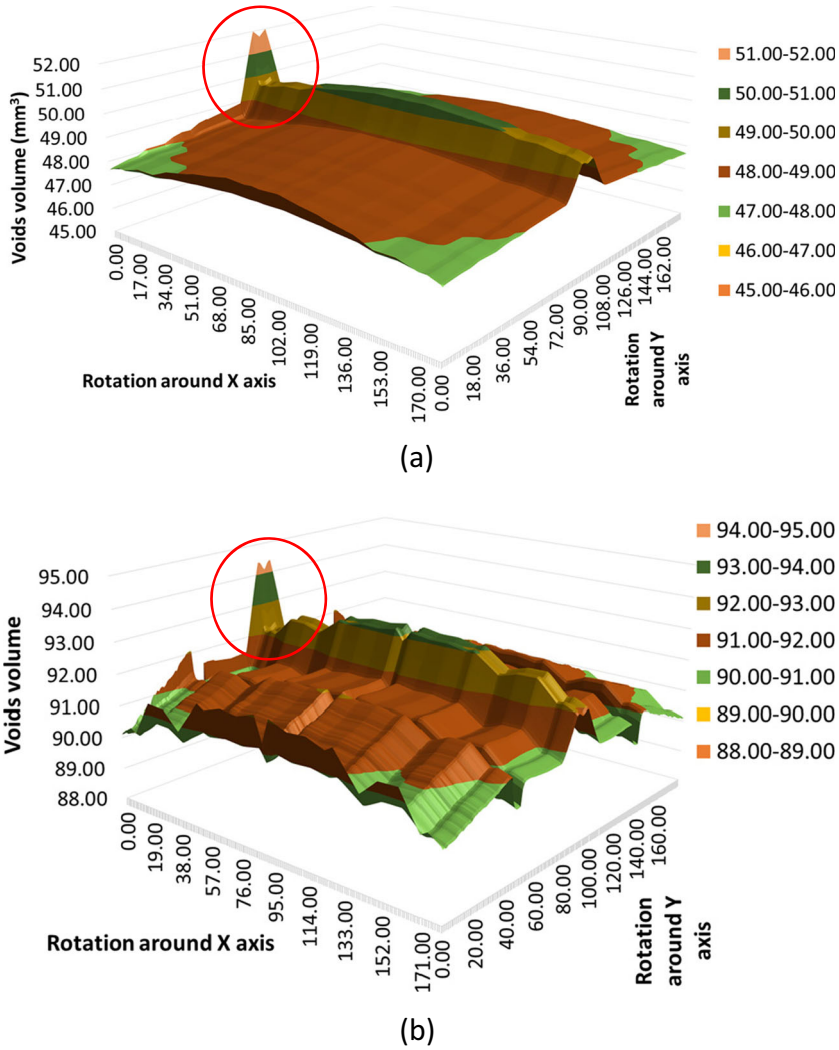

Fig. 29 Voids volume (mm^3) per rotation around X- and Y-axes for valve cover II with allowable overlaps. **a** 50%. **b** 0%

In Fig. 30a, the bounded region in Fig. 28b is expanded. This magnified region illustrates that localized ripples in the void-rotation angle solution surface are apparent. Comparing all voids is computationally expensive. For this specific car seat example, which has a file size of *.stl of 1.62 MB, the algorithm takes approximately 15 h with processor i7-3770, CPU 3.40 GHz, and a 64-bit operating system. Using the same system for this part, and maximizing the overlap for a default orientation, as described in [8], the processing time is 12 min.

The ANOVA results for the car seat case study with both allowable overlap percentage limits (0 and 50%) are summarized in Table 7. The small P values ($P < 0.05$) indicate that the total void areas are dependent on the build rotation. The big F value in the analysis proves that the total voids between rotations are different and build orientations influence voids in the finished part.

Although the small P values in Table 7 statistically confirms the relationship between voids and rotations, methods to determine a global optimum set of solutions is challenging. A heuristic search approach cannot be readily implemented as the bead width, raster angle, and percentage overlap are calculated for each input orientation.

Table 8 shows the total voids with the default toolpath using the Insight® software for the Fortus 400 MC. The selected build orientations in this table are the same as the build orientations presented in Table 6, which are the optimal rotations from this analysis. The default parameters in the OEM software are: (i) 0.254 mm bead height, (ii) 0.5080 mm bead width, (iii) 45°/− 45° raster angle, and (iv) 0% overlap. When comparing the data from Tables 6 and 8, it can be seen that the new model minimizes voids between 3 and 10%. However, the new model avoids contiguous void chimneys.

To explore the solution space options, a frequency analysis comparing the void volumes (void areas multiplied by the slice height) for all rotation variations for the car seat is presented in Fig. 31 when the allowable overlap percentage is limited to 50%. An integer-based exhaustive search approach is taken for this research, which resulted in 360*360 possible rotation angle build solutions studied. For this example, less than 4% of the build

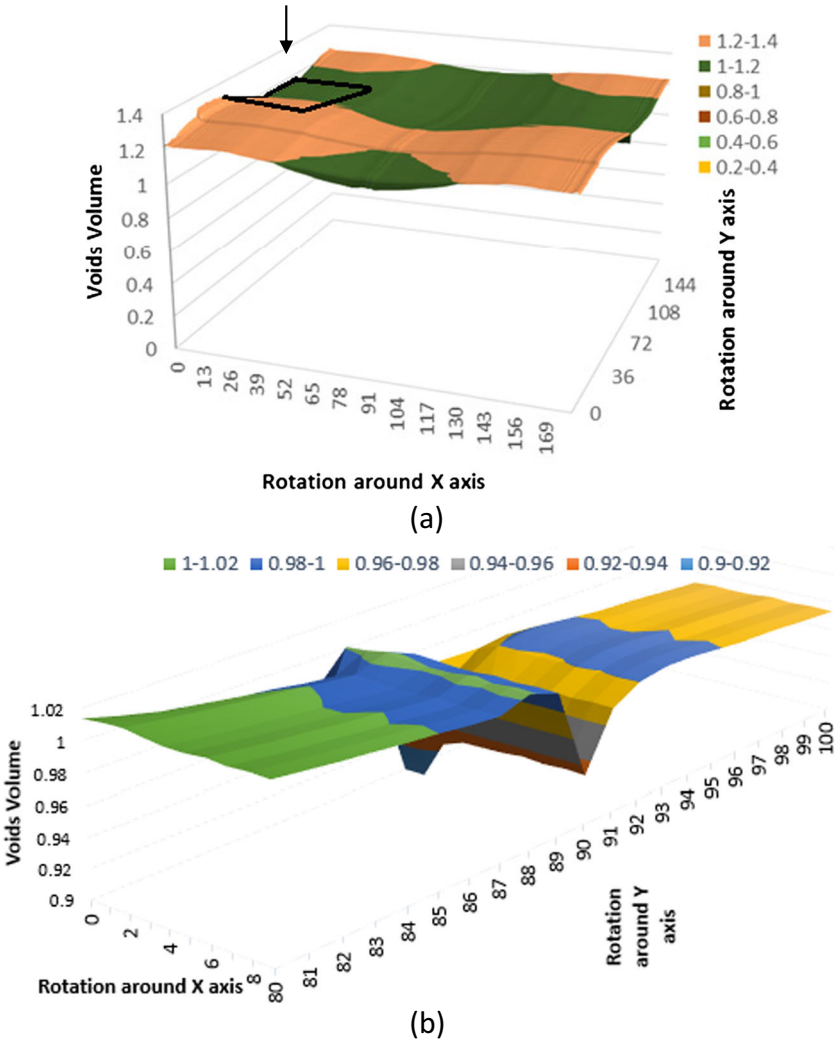

Fig. 30 **a** Voids per rotations and **b** comparing voids in small range of rotations

rotations have a void volume less than 0.91 mm^3. Approximately 19% of the solutions would generate void volumes between 0.95 and 0.97 mm^3, and 9% of the solutions will result in void volumes between 1.05 and 1.13 mm^3. This worst-case condition is 1.5 times less than the default OEM toolpath.

For the car seat, the maximum void volume is 1.1296 mm^3 which occurs for a rotation 39° around the X-axis and 0° around the Y-axis (Fig. 30). For this rotation, there are 106 layers with 0.254 mm bead height. The optimal bead width and overlaps for this rotation is illustrated in Fig. 32b, c. The maximum % overlap is 45%, and the average % overlap is 33%, which is considerably higher than the values derived for best-case orientation (Fig. 24), which are 21% and 11% for the maximum and average overlap % values respectively. Interestingly,

Table 7 ANOVA for car seat case study

Allowable overlaps	Source of variation	SS	df	MS	*F*	*P* value	*F*
50%	Rotation around X-axis	172.2487311	359	0.479801479	84,922.62892	0	1.12
	Rotation around Y-axis	57.669359	359	0.160638883	28,432.33471		
	Error	0.728160388	128,881	5.64987E−06			
0%	Rotation around X-axis	5.130824	359	0.014292	67,267.36	0	1.13
	Rotation around Y-axis	1.81439	359	0.005054	23,787.45		
	Error	0.027383	128,881	2.12E−07			

Table 8 Void volumes with the OEM software for all case studies

	Car seat		Valve cover I		Valve cover II
Rotations (θ_x, θ_y)	(0°, 90°)	(90°, 0°)	(0°, 90°)	(0°, 0°)	(0°, 0°)
Volume of voids (mm^3)	1.67	1.63	147.78	143.63	138.99
Percentage of voids	21.4%	21.1%	14.7%	14.3%	14.5%

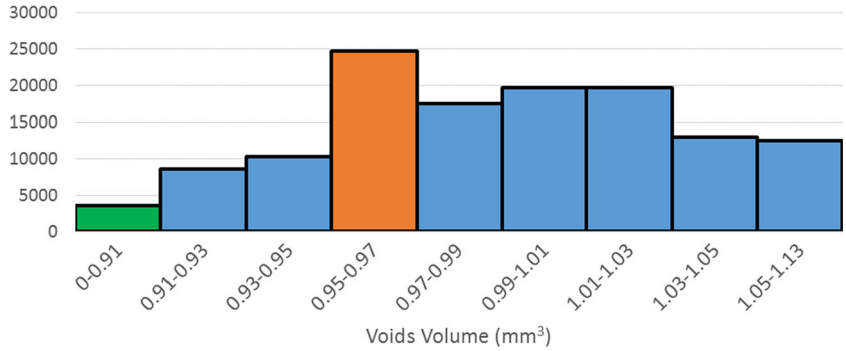

Fig. 31 Frequency of voids with the new model for the car seat case study with 50% allowable overlaps

the bead widths are very consistent for the worst-case orientation, where the maximum bead width is 0.48 mm, and the average bead width is 0.44 mm, but vary significantly for the best-case orientation. Here, the maximum bead width is 0.61 mm, whereas the average value is 0.45 mm.

Figure 33 shows a frequency analysis comparing the void volumes for all rotation variations for valve cover II. For this example, less than 4% of the build rotations have void volumes less than 48.29 mm^3. Approximately 40% of the solution would generate void volumes between 48.65 and 49.01 mm^3, and 4% of the solutions will result in void volumes between 50.1 and 50.46 mm^3. For the best-case scenario, the maximum bead overlap is 21%, the average overlap is 9%, and the maximum and average bead widths are 0.46 mm and 0.42 mm respectively.

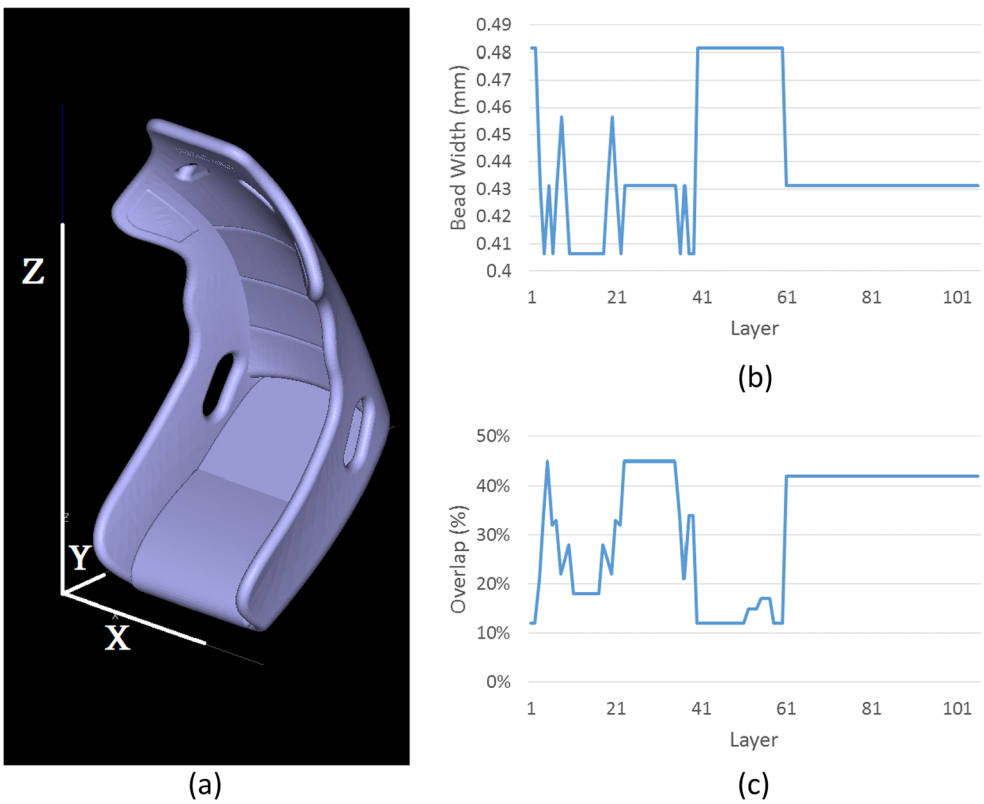

Fig. 32 The worst rotation for the car seat case study, where (**a**) is the 3D model in the worst orientation, (**b**) illustrates the optimal bead width for each layer for this orientation, and (**c**) represents the calculated overlap percentages

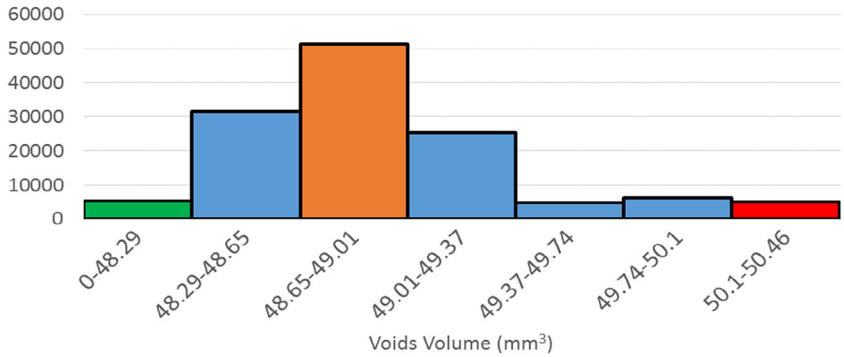

Fig. 33 Frequency of voids with the new model for the valve cover II study with 50% allowable overlaps

Table 9 Summary of the contributions for each phase

Phase	I	II	III
Time	~2 min	~12 min	~15 h
Optimization type	2D	3D	3D
Covers voids		√	√
Derives fill raster angle independent of the machine coordinate system	√	√	√
Maximum overlap boundary condition [8]			
Overlap threshold	√	√	√
Best build orientation			√

It is observed for these case studies that approximately 50% of the available bead width options for a given slice height are utilized and that larger bead widths are utilized for the worse case conditions.

The processing time is long for this optimization strategy. For the car seat, the processing time for the 2D optimization was comparatively short (2 min), whereas the processing time for this methodology was 15 h. The analysis

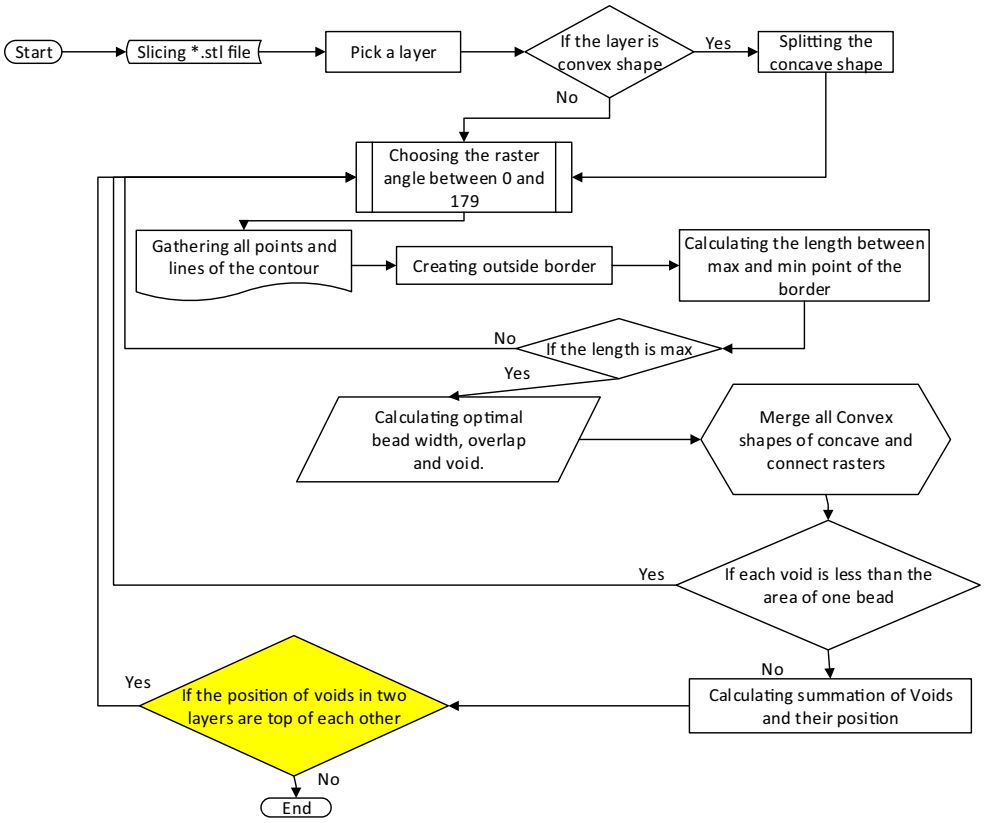

Fig. 34 Exhaustive search algorithm for a generating a minimum void solution

time for the valve covers was approximately 5 days. A summary of the processing time for the three phases is presented in Table 9 for the car seat. Thus, heuristics to reduce the processing time needs to be explored.

6 Summary and conclusions

Due to research related to characterization of mechanical properties for samples built with various AM processes, there is now an understanding of the anisotropic problems with AM processes. However, there is no comprehensive appreciation of the problems associated with the numerous interior voids inherent in the material extrusion processes. Initial research that focused on a local optimization indicated that employing existing build parameters could reduce voids. However, for a global optimization, the impact of the build orientation needs to be evaluated, as well as the characteristics of the solution space. It can be readily seen that most of the solution space (> 90%) will generate a suboptimal result, and significant oscillations are observed for a 0% overlap, which is the default condition for many commercial systems.

The algorithm that is presented in this paper optimizes the build orientation in tandem with the bead width, bead height, percentage overlap, and raster angle, to minimize voids in each layer. The process parameters are discrete variables and have the potential to be unique for each scenario. Void tracking is also performed to prevent an internal chimney, or 3D contiguous voids, from being created, as this will reduce crack propagation sites. The inherent nature of this problem influences the processing time. Once a solution set of options is determined, the users can add more constraints to the model, such as reducing support material requirements, processing time, and surface finish.

The algorithm to find an optimal build orientation with respect to minimizing voids has three phases. Phase I targets minimizing the voids per a build orientation [8]), phase II tracks and manages voids between layers for the same build orientation to ensure that there are no internal chimneys. Phase III consists of an integer exhaustive search, as illustrated in Fig. 34.

This solution approach is industrially relevant for AM software developers or providers and the end users, as it predicts as well as minimizes voids, but it is too computationally intensive. In theory, the solution can be implemented by the software solution providers listed in Table 4, as well as for other AM bead deposition systems such as direct energy deposition, as existing settings and toolpath strategies are being used. However, the processing time is long, and heuristics to reduce the processing time need to be explored.

In the future, experimental tests to validate the relationship between predicted and observed voids (i.e., via CT scans to quantify the void volume fractions for fabricated components for various machine-material sets) and resultant functional properties, such as tensile or comprehensive strength, for each phase needs to be performed. A multi-objective optimization model needs to be developed that considers the following: void minimization, smooth surface finish generation, support material minimization, and build time reduction. Ideally, the user will have all settings predetermined and will fabricate a component that meets functional as well as dimensional requirements.

Acknowledgments The authors would like to thank CAMufacturing Solutions Inc. (especially Bob Hedrick) for their assistance with the C++ programming.

Funding This research is funded by the Natural Sciences and Engineering Research Council of Canada through the Discovery Grant.

References

1. Proto3000 (2016) Fortus400mc. https://proto3000.com/assets/uploads/PDFs/Fortus380450_2015A.pdf. Accessed 26 Feb 2018
2. Schmidt A (2017), Self-supporting angles in large scale additive manufacturing. AES Originals, Large Scale 3D Printing. http://www.additiveeng.com/self-supporting-angles-in-large-scale-additive-manufacturing/. Accessed 26 Feb 2018
3. Cosine Additive (2017) Medium area additive manufacturing (MAAM) handout. https://static1.squarespace.com/static/55627b1be4b020bb00b2d516/t/5734ec36f699bb435295f4b7/1463086144705/CosineAdditive_Handout_AM1Specs-web.pdf. Accessed 3 May 2017
4. Composites Manufacturing (2014) Pros and cons of additive manufacturing. http://compositesmanufacturingmagazine.com/2014/10/pros-cons-additive-manufacturing/2/. Accessed 2016
5. Kishore V, Ajinjeru C, Nycz A, Post B, Lindahl J, Kunc V, Duty C (2017) Infrared preheating to improve interlayer strength of big area additive manufacturing (BAAM) components. Addit Manuf J 14:7–12
6. Cincinnati (2017) SAAM specifications. https://www.e-ci.com/saam-specifications/. Accessed 1 May 2017
7. W. Associates (2014) Wohlers report—3D printing and additive manufacturing state of the industry. Annual Worldwide Progress Report
8. Eiliat H, Urbanic JR (2018) Visualizing, analyzing, and managing voids in the material extrusion process. J Adv Manuf Technol
9. Ahn S-H, Montero M, Odell D, Roundy S, Wright PK (2002) Anisotropic material properties of fused deposition modeling ABS. Rapid Prototyp J 8(4):248–257
10. Onwubolu GC, Rayegani F (2014) Characterization and optimization of mechanical properties of ABS parts manufactured by the fused deposition modelling process. Hindawi Publishing Corporation. Int J Manuf Eng 2014:1–13
11. Rayegani F, Onwubolu GC (2014) Fused deposition modelling (FDM) process parameter prediction and optimization using group method for data handling (GMDH) and differential evolution (DE). Int J Adv Manuf Technol 73(1):509–519
12. Sood AK, Chaturvedi V, Datta S, Mahapatra SS (2011) Optimization of process parameters in fused deposition modeling using weighted principal component analysis. J Adv Manuf Syst 10(2):241–259

13. Vijayaraghavan V, Garg A, Lam JSL, Panda B, Mahapatra SS (2015) Process characterisation of 3D-printed FDM components using improved evolutionary computational approach. Int J Adv Manuf Technol 78(5–8):781–793
14. Vidakis N, Petousis M, Konstantinos S, Vairis A, Athina M, Manolis A (2015) Experimental determination of fused deposition modelling parts compressive strength. 9th International Conference New Horizons in Industry, Business and Education at Skiathos
15. Lee CS, Kim SG, Kim HJ, Ahn SH (2007) Measurement of anisotropic compressive strength of rapid prototyping parts. J Mater Process Technol 187-188:627–630
16. Stucker B, Rosen DW, Gibson I (2010) Additive manufacturing technologies. Springer, ISBN: 978-1-4419-1119-32010
17. Pandey PM, Reddy MV, Dhande SG (2003) Real time adaptive slicing for fused deposition modelling. Int J Mach Tool Manu 43(1):61–71
18. Ledalla SRK, Tirupathi B, SriramV (2016) Performance evaluation of various STL file mesh refining algorithms applied for FDM-RP process. J Inst Eng https://doi.org/10.1007/s40032-016-0303-4, 99, 339, 346
19. Stratasys (2014) FDM Machine. http://www.stratasys.com/. Accessed 12 Jan 2017
20. Kyle Stetz (2009) Makerbot Vs. Dimension SST 1200es. https://kylestetzrp.wordpress.com/. Accessed 26 Feb 2018
21. All 3D (2017). Best 3D printing software tools. https://all3dp.com/1/best-free-3d-printing-software-3d-printer-program/. Accessed August 2017
22. Thompson A, Maskery I, Leach RK (2016) X-ray computed tomography for additive manufacturing: a review. Meas Sci Technol 27(7):1–17